The ESO-Sculptor faint galaxy redshift survey: The photometric sample

S. Arnouts, V. de Lapparent, G. Mathez, A. Mazure, Y. Mellier, E. Bertin, A. Kruszewski

ASTRONOMY & ASTROPHYSICS
SUPPLEMENT SERIES

JULY **1997**, PAGE 163

Astron. Astrophys. Suppl. Ser. **124,** 163-182 (1997)

The ESO-Sculptor faint galaxy redshift survey: The photometric sample⋆

S. Arnouts[1], V. de Lapparent[1], G. Mathez[3], A. Mazure[4], Y. Mellier[1,3], E. Bertin[1,2], and A. Kruszewski[5]

[1] CNRS, Institut d'Astrophysique de Paris, 98 bis, Boulevard Arago, F-75014 Paris, France
[2] European Southern Observatory, Casilla 19001, Santiago, Chile
[3] Observatoire Midi-Pyrénées, Laboratoire d'Astrophysique de Toulouse, URA 285, 14, avenue Edouard Belin, F-31400 Toulouse, France
[4] Laboratoire d'Astronomie Spatiale, B.P. No. 8, F-13376 Marseille Cedex 12, France
[5] Warsaw University Observatory, Al. Ujazdowskie 4, PL-00-478 Warsaw, Poland

Received 22 August, 1995; accepted 18 October, 1996

Abstract. We present the photometric sample of a faint galaxy survey carried out in the southern hemisphere, using CCD imaging at the 3.60 m and NTT-3.5 m telescopes at La Silla (ESO). The survey area is a continuous strip of $0.2° \times 1.53°$ located at high galactic latitude ($b^{II} \sim -83°$) in the Sculptor constellation. The photometric survey provides total magnitudes in the bands B, V (Johnson) and R (Cousins) to limiting magnitudes of 24.5, 24.0, 23.5 respectively. To these limits, the catalog contains about 9500, 12150, 13000 galaxies in B, V, R bands respectively and is the first large digital multi-colour photometric catalog at this depth. This photometric survey also provides the entry catalog for a fully-sampled redshift survey of ~ 700 galaxies with $R \leq 20.5$ (Bellanger et al. 1995a).
In this paper, we describe the photometric observations and the steps used in the data reduction. The analysis of objects and the star-galaxy separation with a neural network are performed using SExtractor, a new photometric software developed by E. Bertin (1996). By application of SExtractor to simulated frames and comparison of multiple measurements, we estimate that the photometric accuracy of our catalog is $\sim 0.05^{\rm m}$ for $R \leq 22$. Then, we use a method to obtain a homogeneous photometric scale over the whole survey using the overlapping regions of neighbouring CCDs. The differential galaxy number counts in B, V, R are in good agreement with previously published CCD studies and confirm the evidence for significant evolution at faint magnitudes as compared to a standard non evolving model (by factors 3.6, 2.6, 2.1). The galaxy colour distributions $B-R$, $B-V$ of our sample show a blueing trend of $\sim 0.5^{\rm m}$ between $21 < R < 23.5$ in contrast to the $V-R$ colour distribution where no significant evolution is observed.

Send offprint requests to: S. Arnouts

⋆ Based on observations collected at the European Southern Observatory, La Silla, Chile.

Key words: galaxies: redshifts; photometry — cosmology: observations

1. Introduction

During the past decade, the photometric and spectroscopic surveys have allowed to improve our knowledge of galaxy formation and evolution. Since the 1980's, the new technology based on CCD detectors has improved the photometric efficiency (sensitivity, linearity, high dynamic range,...) as compared to photographic plates. Although the photographic plates are un-rivaled in their ability to cover large areas of the sky, the large improvements brought by digital surveys, both in the photometric accuracy and in the faint limiting magnitude which can be reached, have allowed important new insight into the properties and the evolution of the different galaxy populations. Several deep digital surveys (Tyson 1988; Lilly et al. 1991; Metcalfe 1991, 1995; Driver et al. 1994; Smail et al. 1995) were performed in different regions of the sky (with a typical field size ≤ 0.012 deg^2) at faint ($B \leq 25$) or very faint magnitudes ($B \leq 27.5$). First, these surveys show that the number-counts of galaxies at $B \simeq 22$ are in excess with respect to a non-evolving model and the disagreement increases with the apparent magnitude. Second, the galaxy colour distributions become significantly bluer at fainter magnitudes.
Several models have been elaborated based on the cosmological parameters (H_0, q_0) and the luminosity function parameters ($L^\star, \Phi^\star, \alpha$) allowing a good fit to the photometric data (see Koof Kron 1992 for a review). Models with pure luminosity evolution where $L^\star$ evolves with look-back time (Bruzual 1983; Guiderdoni & Rocca-Volmerange 1990; Yoshii & Takahara 1988) predict that

the tail of the redshift distribution of very faint galaxies should be extended towards high redshifts. This is not observed in the recent redshift surveys to $B \leq 24$ (Colless et al. 1990, 1993; Cowie et al. 1991; Lilly et al. 1991; Tresse et al. 1994; Glazebrook et al. 1995a), which are in good agreement with the redshift distribution expected for a non-evolving model. Models with number-density evolution (Rocca-Volmerange & Guiderdoni 1990; Broadhurst et al. 1992) are based on a population of dwarf galaxies at $z \sim 0.3$ which would have merged into brighter galaxies by $z \simeq 0$. However, these models are difficult to reconcile with both the recent observations of weak clustering in the correlation function of faint galaxies (Efstathiou et al. 1991 & Roche et al. 1993) and with the physical mechanisms for merging (Ostriker 1990; Dalcanton 1993). The most recent models use a new estimation of the slope α of the local luminosity function (Koo et al. 1993; Driver et al. 1994) which is assumed to increase from $\alpha \simeq -1.1$ to $\alpha \simeq -1.8$ by the presence of a large number of dwarf galaxies (dI, dE). This model is supported by the recent observations of the Medium Deep Survey with the HST to $I = 22$ (Glazebrook et al. 1994b), where the counts of morphologically normal galaxies are well fitted by a non-evolving model and where a large excess of Irregular and Peculiar galaxies is detected which could contribute to the excess of blue galaxies.

Faint photometric and spectroscopic surveys also provide maps of the distribution of galaxies in three dimensions. The nearby surveys show that galaxies are distributed within sharp walls delineating voids with diameters between 20 and 50 h^{-1} Mpc (de Lapparent et al. 1986; Geller & Huchra 1989; da Costa et al. 1994) (where $H_0 = 100$ h km s^{-1} Mpc^{-1}). Very deep pencil-beam surveys were obtained in particular directions of the sky (Broadhurst et al. 1988; Colless et al. 1990, 1993; Cowie et al. 1991; Lilly et al. 1991; Tresse et al. 1994 & Glazebrook et al. 1995a), and in some of these an apparent periodicity on scales of ~ 128 h^{-1} Mpc has been detected (Broadhurst et al. 1990). At these depths ($z \simeq 0.3 - 0.5$), the large amount of time required to obtain the redshift distribution for a complete magnitude-limited sample constrains observations to narrow solid angles. Although the existing deep pencil-beam probes are adequate for establishing the evolutionary history of galaxies, biases caused by sparse sampling may affect the data when used to study the large-scale structures (de Lapparent et al. 1991; Ramella et al. 1992).

In this context, a deep redshift survey near the southern galactic pole was started with the main goal to characterize the large-scale structure at large distances (de Lapparent et al. 1993). The spectroscopic survey covers a continuous solid angle of 0.3 deg^2 and contains ~ 700 galaxies with $R \leq 20.5$ (i.e. $B \leq 22$). The median redshift is at $z \simeq 0.3$. The entry photometric catalogue for the redshift survey was obtained by observing in the B, V, R photometric bands up to 24.5, 24.0, 23.5 respectively in a longer strip of 0.4 deg^2 (this area was not fully covered by spectroscopic observations). The photometric data provide an adequate sample for measuring with a high confidence level the galaxy number counts and the distribution of galaxy colours. The description of the spectroscopic sample of the ESO-Sculptor survey is given in Bellanger et al. (1995a) and the first results about the properties of the large-scale structure are shown in Bellanger & de Lapparent (1995b).

Here we describe in detail the procedures used in the reduction and analysis of the photometric sample. The paper is organized as follows. In Sect. 2, we describe the photometric observations. Sections 3 and 4 outline the data reduction procedures and analyses. In Sects. 5, 6 and 7 we discuss the transformation into astronomical coordinates, the photometric calibration of fields and the magnitude transformations into the Johnson-Cousins standard system. In Sect. 8 we present the method used to match the photometry over the whole survey in each band. In Sect. 9 we show the first results on the star colour distributions, the galaxy colours and the galaxy number-counts. Finally, in Sect. 10 we summarize the major steps of our photometry and we present the scientific perspectives for the near future.

2. Observations

This survey was performed in the context of an ESO-key programme, thus guaranteeing the necessary observing time to perform the full programme. The observations began in 1989 at the 3.60 m telescope and were transferred to the NTT-3.5 m in 1991. At a pace of two observing runs per year, the full time allocation was consumed by the fall 1995. The observing strategy is designed to make optimal use of telescope time. The great advantage of the multi-mode instruments used (EMMI at the NTT, D'Odorico 1990; Dekker et al. 1991, and EFOSC at the 3.6 m, Buzzoni et al. 1984) is the possibility to switch between spectroscopic and photometric observations during the course of the same night, using the same instrument. It allows one to adapt to variable weather conditions: when the conditions are photometric with good seeing quality, priority is given to imaging; if the weather degrades, one can switch to the spectroscopic mode by simple rotation of two wheels placing an aperture mask and a grism into the optical path. Because the number of observing nights is spread over many runs, the imaging data of a given run can be reduced in preparation for the subsequent run, thus yielding finding charts of the galaxies with $R \leq 20.5$ to be observed spectroscopically.

During each run, we observe our main survey region in first priority, and two auxiliary regions at the beginning and end of the night when the airmass for the main survey is large. Here we only report on the data for the main survey region. The data in the auxiliary fields will be used as control samples. The position, galactic latitude and solid

angle of the main field are given in Table 2. In this region of the sky, we acquired $25-30$ frames in each of the B, V, R bands with the 3.6 m telescope. These data cover the right ascension range $0^h19^m00^s < \mathrm{R.A.}_{2000} < 0^h21^m24^s$, and correspond to an area of $\sim 1.53°(\mathrm{R.A.}) \times 0.24°(\mathrm{Dec})$. With the NTT telescope, we acquired $20-25$ frames with $0^h21^m24^s < \mathrm{R.A.}_{2000} < 0^h26^m00^s$ ($\sim 1.00°(\mathrm{R.A.}) \times 0.24°(\mathrm{Dec})$). The $0.24°$ width in declination is covered by 3 EFOSC fields and 2 EMMI fields.

Table 1. Survey characteristics

center R.A., DEC.	b^{II} (deg)	Total area (deg^2)
$0^h22^m30^s$,$-30^\circ 06'$	-83	0.24×1.53

2.1. Instrumentation

Because we performed the photometric observations over a period of six years, different CCD cameras were used over the years to follow the improvement in CCD technology, so that the size and the characteristics of the individual CCD frames vary across the mosaic (made of typically 50 frames in each band). We summarize the principal CCD characteristics in Table 2.1. The first column gives the telescope and instrument used with the different channel for EMMI on the NTT (blue imaging channel: BIMG, and red imaging channel: RIMG). The useful area is the used part of the CCD which differs for large CCDs (LORAL, TEKTRONIX) from the total area because of vignetting.

2.2. Observations

At the 3.60 m telescope with EFOSC, the photometric observations were performed in a range of seeing between 1.10 and 1.65 arcsec. When the FWHM is < 2 pixels, the profile of unresolved objects is poorly sampled, which degrades the star/galaxy separation. With EFOSC, we observed the photometric fields with airmasses between 1.0 and 1.4, and the exposure times for the B, V, R bands are respectively 30 , 25, 20 minutes. The majority of the fields were obtained in only 1 exposure in each band. Bright stars ($R \leq 18$ mag) are thus saturated. Since 1991, we have observed at the NTT with an average seeing of ~ 1.0 arcsec. As the pixel size of the CCDs is smaller, we have a better sampling of the p.s.f. and therefore our star/galaxy separation is limited by seeing. The airmasses are also in the range $1.0-1.4$. The exposure times for the B, V, R bands were respectively 25, 20, 15 minutes. To avoid saturation of the CCDs by bright stars, the images are summed from 2 or 3 exposures. The photometric strategy adopted to probe the different strips is to obtain a mosaic of CCD frames regularly offset by $\frac{9}{10}$ of the CCD size providing many overlaps for subsequent checks of the photometry. In Table 2.1, we summarize the characteristics of the photometric observations during the different runs. For each run, the photometric zero-points (apparent magnitude of a star with an absolute magnitude $M = 0.$ and null color term exposed during 1 second, as defined in Eq. (1)) are given.

3. Data pre-reduction

Before the photometric analysis, the raw data are reduced using the MIDAS environment in the following steps:
bias subtraction, skimming subtraction (for RCA CCD #8), flat-fielding and cosmic-ray removal.

3.1. Bias subtraction

A "master" bias frame is obtained by averaging over ~ 50 frames from which cosmic ray events have been removed. As the bias level varies with time, the bias subtraction for each scientific frame is performed in two steps:
(1) Subtraction of the master bias frame.
(2) Subtraction of the mean difference between the overscan of the scientific frame and that of the master bias frame.

3.2. Skimming subtraction

With RCA CCD #8, the raw CCD frames have a skimming pattern, characterized by systematic column intensity offsets across the entire CCD. This pattern varies in intensity at low illumination levels and becomes constant above ~ 1000 adu, well below the sky level of all our scientific frames but above that for the photometric calibration frames. Because the skimming offsets are additive biases, we can calculate them by using flat-field frames with different illumination levels. Scaling and subtraction of two flat-field frames with different exposure times yield a preliminary skimming frame. As the skimming feature is stable along each column, the signal to noise is improved by replacing each pixel of a column by the mean value along the column. The mean level of the entire skimming frame is then adjusted to be zero. A set of skimming frames derived from pairs of flat-field frames with increasing illumination levels are calculated. Then for each science frame, the appropriate skimming frame can be subtracted. The skimming subtraction is important for the calibration frames where the sky level is very low. To preserve the quality of our photometry, the calibration frames for which we cannot adequately subtract the skimming pattern are rejected.

3.3. Flat-fielding

The flat-field frame provides a map of the sensitivity variations over the CCD chip. This map depends on the

Table 2. CCD characteristics and photometric observations

Telescope/instrument	CCD	Pix size ($''$/pix)	Useful area (arcmin^2)	Period	Average zero-points		
					B	V	R
3.60 m/EFOSC	RCA#8	0.675	3.7×5.7	$43-44$	23.70 ± 0.03	24.24 ± 0.04	24.21 ± 0.02
3.60 m/EFOSC	RCA#8	-	-	$45-46$	23.41 ± 0.01	24.06 ± 0.03	24.03 ± 0.02
NTT/EMMI (RIMG)	THX#18	0.44	7.5×7.5	$49-50$		24.30 ± 0.02	24.65 ± 0.03
NTT/EMMI (RIMG)	LOR#34	0.35	9.3×8.8	52	24.69 ± 0.02[1]		25.14 ± 0.02
NTT/EMMI (RIMG)	TEK#36	0.27	9.1×9.1	54		25.40 ± 0.02	
NTT/EMMI (BIMG)	TEK#31	0.37	6.2×6.2	52	24.69 ± 0.02		
NTT/EMMI (BIMG)	TEK#31	-	-	54	24.26 ± 0.01		

spectrum of the incoming light. As the flat-field pattern is stable from night to night, we obtain for each observing run a "super flat-field" in each filter band by doing a median filtering of all the scientific frames obtained during the run. The median filtering removes the objects from the images and yields the large-scale sensitivity variations. This is the best flat-field frame which can be obtained, because it is derived from the sky on the science frames themselves. The number of frames must be sufficient to create a high signal-to-noise final flat-field frame. In practice, because our fields are sparsely populated, the super flat-field results from the median filtering of 5 to 20 science frames (depending on the observing run). This flat-field is normalized and is divided into each data frame. The large-scale residual variations in the background of each flat-fielded frame are $< 1\%$.

3.4. Summation of multiple exposures

After flat-fielding, we align multiple exposures of identical fields using several unresolved objects, sum the individual exposures and calculate the mean airmass for the final frame.

3.5. Cosmic ray removal

To remove cosmic rays from the summed frame, we apply a filtering algorithm kindly provided by P. Leisy. Each pixel is compared with the mean of the 5×5 neighbouring pixels. If the pixel value differs by more than 5σ from the mean, it is replaced by the mean value. The value of 5σ is large enough to prevent the subtraction of real objects.

4. Photometric analysis

This section briefly describes the photometric software used in the data analysis (SExtractor: Source Extraction software). A complete description is given in Bertin & Arnouts (1996, hereafter BA96).

4.1. Description of photometric package

The photometric analysis is done in four steps:

4.1.1. determination of the sky background

The background map is derived by binning the frame into large meshes (32×32 or 64×64 pixels), and removing the possible overestimations due to bright objects using a κ-sigma clipping algorithm. This sky background map is subtracted from each frame.

4.1.2. Detection of objects

The detection algorithm determines a group of connected pixels above a given threshold. A minimum number of connected pixels is chosen in order to avoid spurious objects (bad pixels, un-removed cosmic rays,...). Convolution with a gaussian with a FWHM close to the seeing improves the detection of objects by decreasing the background noise. The typical threshold used is 1.2σ above the background value (σ is measured from the unsmoothed background) corresponding to a surface brightness equal to 27 mag arcsec^{-2} in B, 26.5 mag arcsec^{-2} in V and 26 mag arcsec^{-2} in R. When such a low threshold is used, large spurious faint objects can appear in the wings of objects with shallow profiles. This effect is seen around elliptical galaxies or bright stars where the local background noise increases and can exceed the detection threshold. A cleaning procedure is therefore applied to check if the detected objects are real. For the faint objects in the vicinity of bright objects, a new estimation of the local background is obtained by assuming that the dominant central object has large gaussian wings. If the mean surface brightness of the faint object is lower than the calculated local threshold, the object is rejected.

4.1.3. Deblending of neighbouring objects:

Each detection of a connected set of pixels is processed through a deblending algorithm based on multi-thresholding as described in BA96.

4.1.4. Photometry

Three kinds of magnitudes are used: isophotal, "corrected isophotal"and "adaptive aperture".

The "corrected isophotal" retrieves the lost flux in the isophotal magnitude by assuming that the wings of objects outside the limiting isophote are nearly gaussian (see Maddox et al. 1990a). This estimation of the "total" magnitude could be improved by assuming that the profile of objects follows the more realistic Moffat profile. However, if the value of the threshold is low, the gaussian profile provides an adequate correction as demonstrated by the tests on simulated frames (see Sect. 4.2).

The "adaptive aperture" magnitude is the best estimation of the "total" magnitude. The algorithm is similar to the "first-moment" measure designed by Kron (1980). This magnitude is calculated in two steps:

(1) The object's light distribution above the isophotal threshold is used to measure an isophotal elliptical aperture characterized by the elongation ϵ and position angle θ.

(2) The first moment r_1 is calculated in an aperture $2\times$ larger than the isophotal aperture in order to reach the light profile information below the isophotal threshold.

The first moment is used to define the "adaptive aperture" of radius kr_1 inside which we measure the "total" magnitude. The principal axes of each object are defined by ϵkr_1 and kr_1/ϵ. Kron (1980) uses a circular aperture of radius kr_1 with $k=2$ which measures 90% of the total flux from the objects. To converge near the "total" magnitude we can increase the k value, but a compromise must be found between the added measured flux and the increasing noise in larger apertures. As Metcalfe et al. (1991), we choose $k=2.5$, yielding 94% of the total flux inside the adaptive aperture (this value was calculated using simulated frames with a large variety of galaxy profiles). In contrast to the isophotal magnitude which operates at fixed signal-to-noise, the "adaptive aperture" magnitude may be determined at very low signal-to-noise. Sometimes for faint objects, r_1 may converge to erroneously small apertures. We therefore constrain the apertures to a minimum value of $R_{\rm min}\sim 3.5\sigma_{\rm ab}$ (where $\sigma_{\rm ab}$ is the mean standard deviation of the bivariate gaussian profile defined by the second order moments of the object profile (BA96)).

4.2. Simulations

To test the quality of the photometry for objects with different magnitudes, we use simulated frames provided by E. Bertin (BA96) and generated according to the following scheme. A sky background is defined by a sky surface brightness ($\mu_R=21$ mag/$''^2$), and Poisson noise is added according to a gaussian distribution as observed on real CCD frames. A set of stars with a Moffat profile (Moffat 1969) are generated. Galaxies are produced with a large variety of shapes and sizes. The pixel size and seeing disk are adjusted to resemble as much as possible the real frames. The frames are defined through the R band corresponding to the band used here for the selection of the spectroscopic sample and for the star/galaxy separation. The results of the tests on several simulated images are based on ~ 6000 galaxies and ~ 600 stars in total.

4.2.1. Test of photometric accuracy

In Fig. 1, we compare the mean difference between the different measured magnitudes and the true magnitude for the galaxies. The mean difference is calculated in bins of $0.5^{\rm m}$ of the true magnitude. The error bars represent the rms scatter around the mean.

As expected, the isophotal magnitude which measures the flux inside the defined isophote looses the flux in the wings outside this isophote. Figure 1 shows that an increasing fraction of flux is lost for fainter magnitudes. The "corrected isophotal" magnitude (defined in Sect. 4.1.4) provides a significant improvement.

Figure 1 also confirms that the "adaptive aperture" magnitude (Kron magnitude) measures $\sim 94\%$ of the flux of objects over the entire magnitude range (the systematic offset of $0\overset{\rm m}{.}06$ is indicated by the dashed line in Fig. 1). To reach the "total" magnitude, we then subtract a constant value of $0\overset{\rm m}{.}06$ to all magnitudes. The error bars in Fig. 1 are $\sim 0.05^{\rm m}$ for galaxies with $R\leq 21.$, and up to $\sim 0.2^{\rm m}$ at fainter magnitudes. The interest of the "adaptive aperture" magnitude over the isophotal magnitude originates in it insensitivity to seeing and redshift (Kron 1980).

Because a large fraction of the detected objects in our survey are stars, we also compare in Fig. 2 the different magnitudes for the simulated stars. Even when a gaussian profile is used to correct the flux lost in the wings of stellar objects with Moffat profile, the "corrected isophotal" is very close to the total magnitude for $R\leq 23.5$.

Because the fraction of flux measured in a fixed aperture is constant for stars, we check the reliability of the second order moments by comparing the "adaptive" magnitudes to the "aperture" magnitudes. The aperture radius is defined by $3.5\times\sigma_{\rm a}$ where $\sigma_{\rm a}$ is the second order moment along the major axis, estimated by using unsatured stars with high signal-to-noise (typically $19^{\rm m}\leq R\leq 22^{\rm m}$). The lost flux is stable in the full magnitude range and is close to $0.04^{\rm m}$. This value is in good agreement with the "adaptive" aperture obtained by using a minimum radius defined as $3.5\,\sigma_{\rm ab}$ (where $\sigma_{\rm ab}=\sqrt{\sigma_{\rm a}.\sigma_{\rm b}}$ is calculated for each object). We can then conclude that the second order moments can be reliably estimated down to very low signal-to-noise ratios and the "adaptive" magnitude is a good measure of the total magnitude.

Despite the reliability of "adaptive" magnitude for stars, we use the "corrected isophotal" magnitude as being the best magnitude to estimate the "total" magnitude. Because, we make the star/galaxy separation only for $R\leq 22^{\rm m}$, we use the "corrected isophotal" magnitude up to this cut-off for the stellar sample and the "adaptive" magnitude for the galaxy sample. At fainter magnitudes,

no classification is done, thus we use the "adaptive" magnitude for all objects.

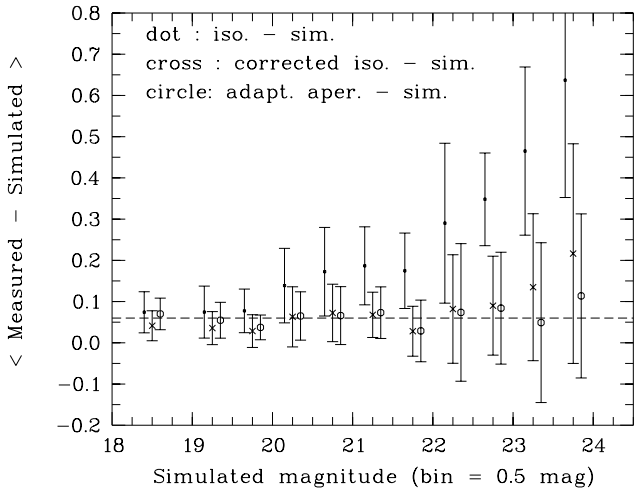

Fig. 1. Mean difference in $0.5^{\rm m}$ bins between the measured magnitudes and the true magnitudes for galaxies in simulated R frames. The symbols for the different magnitudes used are given inside the graph. The error bars show the rms scatter around the mean. The dashed line represents the expected position of magnitude difference for the "adaptive aperture" magnitude corresponding to the 94% enclosed flux

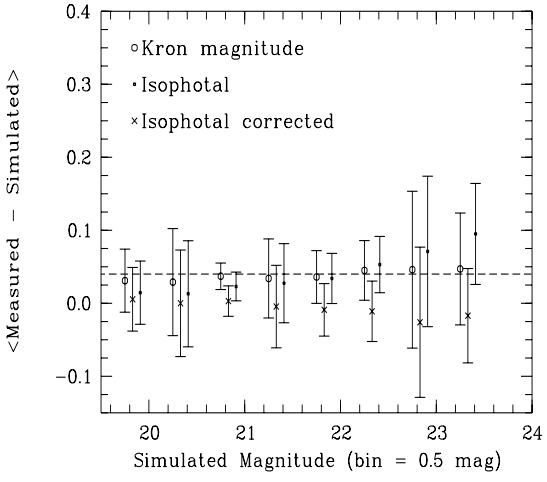

Fig. 2. same as Fig. 1 for stars. The dashed line represents the flux measured inside a radius defined as $3.5 \times \sigma_{\rm a}$, where $\sigma_{\rm a}$ is derived from stars with high signal-to-noise (as described in text)

4.2.2. Conclusion

The results of the tests applied to the simulated images show that:

(1) For galaxies, the "adaptive aperture" magnitude is a robust estimate of the "total magnitude" (after correction for an offset of $0.06^{\rm m}$) down to $R \leq 24.0$. The uncertainty in the measure is close to $0.05^{\rm m}$ up to $R \leq 21$ and increases to $0.2^{\rm m}$ up to $R \leq 23.5$. However, this is an aperture magnitude and it is sensitive to crowding by close neighbours. Therefore, when an object has a neighbours closer than 2 isophotal radii, we use by default the "corrected isophotal" magnitude.

(2) For stars, the "corrected isophotal" magnitude is a reliable estimate of the "total magnitude" for $R \leq 23.5$.

(3) Because we measure "total" magnitudes, the colours can be calculated as the difference between the "total" magnitudes in each passband. The colour error can be estimated as the quadratic sum of the error in each band. For objects brighter than $R \leq 22$, the colour error is $\simeq 0.07^{\rm m}$ and at fainter magnitudes the colour error is $\simeq 0.28^{\rm m}$.

4.3. Star-galaxy separation

To build the spectroscopic catalogue, it is important to exclude the stellar objects. The star/galaxy separation is performed using the neural network included in the photometric software SExtractor. For a complete description of the principle, the training (with using simulated frames containing stars and galaxies), and various tests of this neural network, the reader can refer to BA96. Here, we describe the input and output parameters used for the separation. For each image, the classifier works in a ten-parameter space containing 8 isophotal areas defined by dividing the peak intensity in 8 levels equally spaced in logarithmic scale, the central peak intensity, and one control-parameter which defines the fuzziness of the frame and is chosen to be the seeing (in pixels). This set of input parameters is shown to provide an "optimal" description of the characteristics of each image (BA96). The neural network provides an output parameter defined as a "stellarity-index". Because the p.s.f. of a frame is the parameter which determines the quality of the performance of the neural network, SExtractor estimates on each frame the FWHM of the p.s.f. using the unsatured bright stars and uses it for the neural network. The "stellarity-index" output parameter is a measure of the confidence level in the classification of each image. The value varies between 1 for stars and 0 for galaxies. In Fig. 3, we show the stellarity index as a function of magnitude for a R frame. For our 50 R frames, a reliable classification can be done for $R \leq 22$ with a success rate for the galaxies close to 95% (BA96). A fainter magnitude limit can be reached for several frames with good seeing quality (such a frame is shown in Fig. 3). To be sure that galaxies are not

mis-classified as stars, we define as stars all objects with a stellarity index greater than 0.8. The corresponding magnitude limit for classification is 1.5 magnitude deeper than our spectroscopic limit of $R = 20.5$, and thus guarantees that our spectroscopic sub-sample is poorly biased by misclassified objects.

Figure 3 shows that at faint magnitudes $R \geq 23$, the stellarity index approaches 0.5 because no distinction can be made between the two classes when the profiles are dominated by the seeing disk. On the other hand, at bright magnitudes, for the largely saturated stars ($R \leq 16$) the stellarity index may drop below 0.8.

When we started the spectroscopic observations, the photometric software by E. Bertin was not avalaible. We thus used INVENTORY, the photometric software developed by A. Kruszweski (West & Kruszewski 1981) and avalaible in the MIDAS environment. INVENTORY provides a reliable star-galaxy separation for $R \leq 21$ and was used to generate the entry catalogue for the first half of the spectroscopic observations. The good success rate in the separation is confirmed by only 15 spectra of stars observed out of a total number of 521 reduced spectra (i.e. $\leq 3\%$) (Bellanger et al. 1995a).

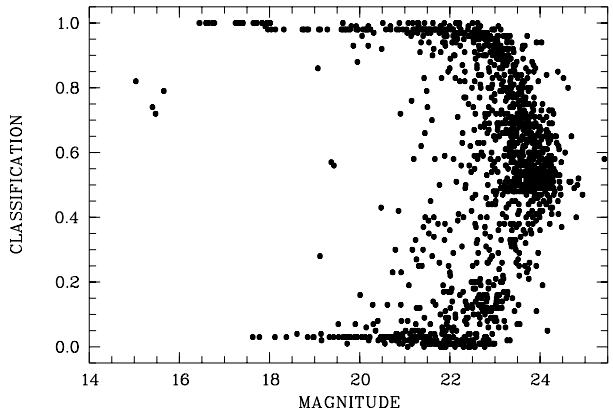

Fig. 3. Star/galaxy separation for a science frame observed in the R band with a seeing of 0.9 arcsec. The ordinate shows the output parameter of neural network, the "stellarity index" which provides an estimate of the confidence level in the classification of each object as a star (CLASS = 1) or a galaxy (CLASS = 0)

5. Astronomical coordinates

To obtain precise astrometry for the detected objects in our CCD frames, the regions of the SERC-J photographic plates containing our survey were digitized at the MAMA ("Machine Automatique à Mesurer pour l'Astronomie" at Paris Observatory) which is developed and operated by CNRS/INSU (Institut National des Sciences de l'Univers).

The astrometry is performed in two steps.

(1) By alignment of the images of the digitized plates onto our CCD frames (using existing MIDAS commands applied to objects in the field), we are able to derive the coordinate transformation equations from CCD to photographic plate. There is one set of transformation equation for each CCD frame.

(2) The transformation equations from photographic plate to equatorial coordinates are provided by the MAMA facility as FORTRAN programs. The astrometric reduction uses the PPM catalogue (Roeser & Bastian 1991).

(3) Combination of the two transformations yields for each CCD frame the transformation equations from pixels to equatorial coordinates. We use a set of MIDAS procedures which were written with the goal to perform the transformation routinely for the numerous fields of the programme (Revenu & de Lapparent 1992).

The overlapping regions of neighbouring CCD frames allow us to estimate the internal astrometric consistency. In Fig. 4, we plot the median position difference defined as $\sqrt{\cos^2(\mathrm{DEC}_0) \times (\mathrm{RA}_0 - \mathrm{RA}_1)^2 + (\mathrm{DEC}_0 - \mathrm{DEC}_1)^2}$ in bin sizes of 1 mag. The NTT observations are represented by dots and those from the 3.60 m by crosses. The error bars are the 1 σ dispersion measured in each magnitude bin. For the NTT, the differences of median position vary from $0.1'' \pm 0.1''$ for $R \leq 22$ to $0.2'' \pm 0.3''$ for $R \leq 24$, and from $0.2'' \pm 0.2''$ for $R \leq 20$ to $0.4'' \pm 0.3''$ for $R \leq 24$ with the 3.60 m. The better accuracy for the NTT fields is due to the better sampling (smaller pixel size) which improves the measurement of the central position of the objects: the seeing disk is spread over ~ 3 pixels for NTT frames, whereas it is spread over only ~ 2 pixels for 3.60 m frames.

6. Calibration

To calibrate our CCD magnitudes into the Johnson B, V and Cousins R standard system (hereafter B, V, R), we observed the faint standard star sequence NGC 300 from Graham (1981) and the bright standard star sequences MARKA, NTPHE, PG0231, SA92 from Landolt (1992). Several sequences were observed each night in order to obtain a zero-point for each night. We use the following linear transformation equations to convert instrumental magnitudes m_{ccd} into standard magnitudes M_{std}:

$$M_{\mathrm{std}} = m_{\mathrm{ccd}} - A_M \times \sec\xi + k_{\mathrm{M}} \times \mathrm{COLOUR} + C_{\mathrm{M}} \qquad (1)$$

where M_{std} define the standard magnitudes and $\mathrm{m_{ccd}}$ define the instrumental magnitudes (in adu s^{-1}) through respectively the three filters B, V, R. The colour term COLOUR is the standard colour provided by Graham or Landolt $B-V$ or $V-R$. The instrumental CCD magnitude of standard stars is calculated as the "corrected isophotal"

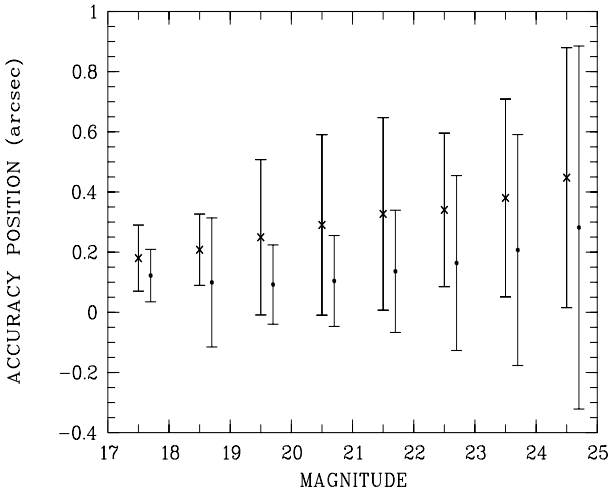

Fig. 4. Mean difference in arcsec in the astrometric position of common objects in CCD overlaps as a function of R magnitude in bin sizes of 1 mag. The data for the NTT and 3.60 m telescopes are represented by dots and crosses respectively. The error bars show the 1 σ rms dispersion

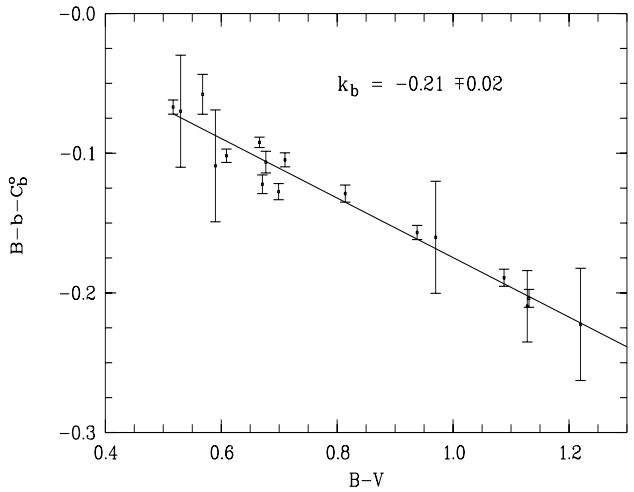

Fig. 5. Colour term as a function of colour for standard star sequences of an entire observing run (NTT/EMMI-B, CCD TEK#31). The error bars for each star is the quadratic sum of the instrumental error resulting from several measurements and the intrinsic error given by the authors. The solid line represents the weighted least-squares regression whose slope provides the value of $k_{\rm B}$. The $C_{\rm b}^0$ are chosen for each set of stars of each night to minimize the scatter in the colour term $k_{\rm b}$

magnitude (see Sect. 4.2.1), thus yielding a good estimation of the total magnitude.

The extinction coefficients $A_{\rm M}$ for the different filters B, V, R are derived from the La Silla extinction curve provided in the ESO manual (Schwarz & Melnick 1993).

The zero-points $C_{\rm M}$ are specific to each combination of Telescope/Instrument/ CCD/Filter/atmospheric conditions. These are easily measured using a large number of standard stars observed each night (see Fig. 6). The colour coefficients $k_{\rm M}$ allow the magnitudes from the "observing" filter (resulting from the Telescope/Instrument/CCD/Filter combination) to be corrected into the B, V, R standard filters. We assume that they remain constant during each observing run, and use the calibrations of an entire run to calculate these coefficients. Two color coefficients for the V band can be calculated depending on whether $B-V$ or $V-R$ colours are used (denoted k_{V_B} or k_{V_R} respectively).

In practice, we estimate the colour coefficients for each different configuration of Telescope /Instrument / CCD /Filter as shown in Fig. 5. The resulting colour coefficients are shown in Table 3. The quoted errors are the rms. uncertainties in the linear fit. The measured colour coefficients are then used to determine the accurate zero-point $C_{\rm M}$ for each night.

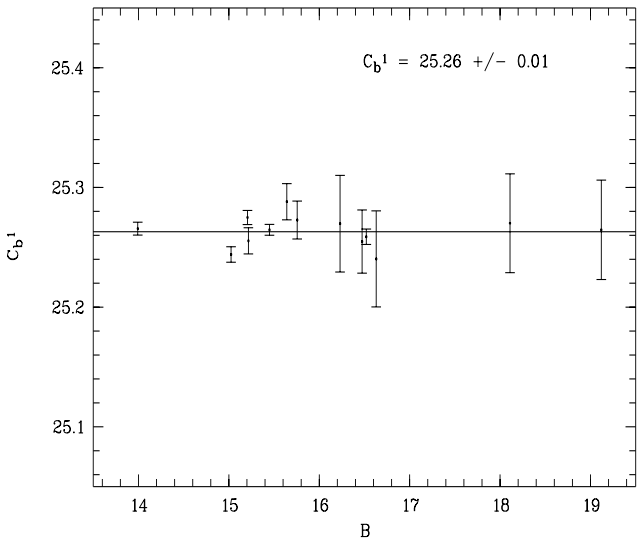

Fig. 6. Resulting zero-point value $C_{\rm b}^1$ for one observing night using the color coefficient $k_{\rm B}$ calculated in Fig. 5. The error bars for stars are the same as in Fig. 5, and the zero-point is calculated by weighted least-squares regression by a constant term

Table 3. Measured colour coefficients

Inst/CCD	k_B	k_{V_B}	k_{V_R}	k_R
EFOSC/RCA#8	$0.16 \pm .03$	$0.04 \pm .02$	$0.10 \pm .02$	$0.00 \pm .02$
EMMI-R/THX#18		$0.05 \pm .01$	$0.10 \pm .02$	$-0.10 \pm .01$
EMMI-R/LOR#34				$-0.03 \pm .01$
EMMI-R/TEK#36		$0.03 \pm .02$	$0.05 \pm .02$	
EMMI-B/TEK#31	$-0.21 \pm .02$			

7. Standard magnitudes

7.1. Transformation equations

The calibration of the five different CCDs used in the imaging survey allows us to derive a homogeneous set of standard magnitudes for all detected objects. Instrumental magnitudes are related to standard magnitudes by the transformation Eq. obtained from Eq. (1):

$$M_{\rm std} = M_{\rm ccd} + k_{\rm M}(B-V). \quad (2)$$

where $M_{\rm ccd} = m_{\rm ccd} - A_{\rm M}{\rm sec}\xi + C_{\rm M}$.
We assume that no correction for galactic absorption is necessary because our fields lie at high galactic latitude $b^{II} \sim -83^\circ$ and the widest extent of the full survey is only 1.53 deg.
Because we have a priori no knowledge of the colours of the detected objects in the Johnson-Cousins system, we invert the set of Eq. (2) so that the colour correction appears in terms of *observed* colour. We give the equations for the V band where two colour coefficients are measured:

$$V = V_{\rm ccd} + \frac{k_{V_B}}{1-k_B+k_{V_B}}.(B_{\rm ccd}-V_{\rm ccd}) \quad (3)$$

$$V = V_{\rm ccd} + \frac{k_{V_R}}{1-k_{V_R}+k_R}.(V_{\rm ccd}-R_{\rm ccd}). \quad (4)$$

Most objects detected in one filter are identified in the other 2 filters (see next subsection). For the galaxies detected in only one filter, we derive the magnitudes in the other filters using the standard colours $B-V=1.0$ and $V-R=0.5$. These mean values are derived from the mean galaxy colours obtained for the survey and reported in Sect. 9.2.2. To check the reliability of our colour coefficients listed in Table 3 and the resulting standard magnitudes, we estimate V in two possible ways using Eqs. (3) and (4). The mean differences in the 2 corresponding magnitudes for 7000 objects observed at the NTT and 5000 objects at the 3.60 m are $\leq 0.005 \pm 0.001$ mag. This test demonstrates the reliability of our measured colour coefficients. Because the R and V frames cover almost the same area of the sky, the final V magnitudes are calculated in terms of $V-R$ colour (Eq. 4).

7.2. Colour completeness

Although R and V frames cover almost the same area of the sky, the B frames cover only about 80% of area observed in R and V, partly because of the smaller CCD size in the EMMI blue channel. Within the common area of the B, V and R bands, we define a colour completeness rate for objects selected in the B band as the fraction of B detected objects with associated V or R or both detections (in bins of 1 mag). We calculate the analogous curves for the V and R bands inside the same area. These various curves are shown in Fig. 7. Typically, the completeness drops below 90% 1 mag brighter than the limit of the catalogue in each band. At the limit of the spectroscopic catalogue $R \leq 20.5$, the completeness in B and V is greater than 95%.

8. Matching CCD overlaps

Because our images were taken over a 6-year period using different telescopes (3.60 m and NTT), instruments (EFOSC2 and EMMI) and CCDs (different pixel size and color coefficients), it is crucial to adjust the zero-points of our magnitude scales over the whole survey. This is done by comparing the measured magnitudes of objects located in the overlapping edges of the CCD images (1/10 of the CCD size, i.e. ≤ 1 arcmin). This adjustment guarantees an internally homogeneous photometry, and corrects for the systematic offsets in the photometric calibrations from one observing night/run to another, as well as other possible variations not accounted for like the systematic variations in the extinction curves due to the eruption of the Pinatubo volcano in 1991 (Burki et al. 1995).
The input images have the standard magnitudes derived in Sect. 7, and the equatorial coordinates (α, δ) described in Sect. 5. Because the overlaps contain few objects, we use all stars and galaxies with $R < 22$ mag. The magnitudes can then be directly compared in the overlaps of each CCD, and we show below how the mean offsets provide the correction of zero-point to apply to each CCD.

8.1. Method

Because each CCD frame has 2 to 4 overlaps, the adjustment of zero-points must be done by a global least-squares fit. We use the method described by Maddox et al. (1990a) and originally proposed by Seldner et al. (1977). Seldner designed this method for adjustment of galaxy counts in the overlapping cells on neighbouring plates to correct the systematic variations in the magnitude limits from plate

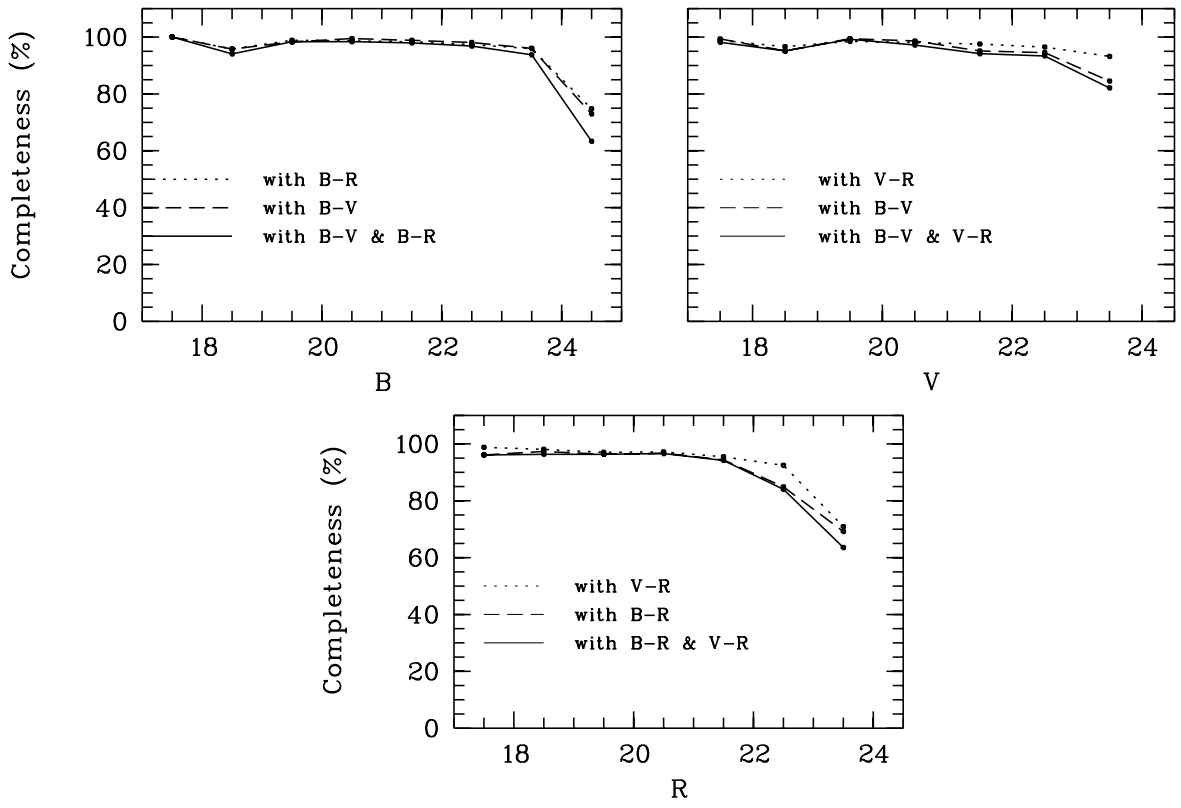

Fig. 7. Colour completeness of B, V and R detected objects in $B-V$ and $V-R$ colours. The completeness is estimated in bin sizes of 1 mag. The coding of the curves is specified inside the graph

to plate. Instead of comparing the counts, Maddox formalism allows to compare the differences of magnitude for common objects on overlapping photographic plates. For a complete description of the technique the reader can refer to Maddox et al. (1990a). Here we briefly review the principle of the method.

For each galaxy k on CCD i, we define a correction for the zero point δC_i by

$$m_0^k = m_i^k + \varepsilon_i + \delta C_i \tag{5}$$

where m_0^k is the "true magnitude" and m_i^k is the measured magnitude with an error ε_i. On each overlapping CCD pair (i,j), we obtain

$$m_0^k = m_i^k + \varepsilon_i + \delta C_i = m_j^k + \varepsilon_j + \delta C_j. \tag{6}$$

We define a mean offset $\overline{T}_{ij}$ so that

$$\overline{T}_{ij} = < m_j^k - m_i^k > \simeq \delta C_i - \delta C_j \tag{7}$$

here, we assume that $< \varepsilon_i > = < \varepsilon_j > = 0$. Because the CCD provides a linear response in a large magnitude range, $\overline{T}_{ij}$ is independent of the magnitude $(m_j + m_i)/2$. We thus measure $\overline{T}_{ij}$ by an offset in the zero$^{\rm th}$ order of $(m_j - m_i)$ versus $(m_j + m_i)/2$ (for the photographic plates, Maddox et al. (1990a) define $\overline{T}_{ij}$ by a third order adjustment). Figure 8 shows an example of the differences of magnitudes for all objects in one overlap $(i,\ j)$. We require that the overlaps taken into account in the equation system have more than 5 objects in order to guarantee a reliable measure of the mean offset value.

For CCD i, we obtain several correction factors corresponding to each of its neighbours j which we denote as

$$\delta C_i = \delta C_{i_j} = \delta C_j + \overline{T}_{ij} \qquad\qquad j \subset i \tag{8}$$

where δC_{i_j} is the correction factor estimated with neighbouring CCD j, and $j \subset i$ denotes all the neighbours j of CCD i.

The goal is to determine the unique value δC_i for CCD i which globally minimizes the scatter in the δC_{i_j}. These coefficients are calculated by minimization of the function F defined by:

$$F = \frac{1}{2} \sum_i \sum_{j \subset i} W_{ij} (\overline{T}_{ij} + \delta C_j - \delta C_i)^2 \tag{9}$$

where $W_{ij} = 1/\mathrm{var}(T_{ij})$ are the weighting factors which favor the overlaps with a small variance.
With $\frac{\partial F}{\partial \delta C_i} = 0$, we obtain the following set of equations:

$$\delta C_i^{n+1} = \frac{\sum_{j \subset i} (\delta C_j^n + \overline{T}_{ij}) W_{ij}}{\sum_{j \subset i} W_{ij}} \quad (10)$$

which are solved by iteration. To increase the convergence speed and the stability of this iterative method, we adopt the technique from Maddox of adding the previous value δC_i^n into Eq. (10):

$$\delta C_i^{n+1} = \frac{\left(\delta C_i^n W_{ii} + \sum_{j \subset i} (\delta C_j^n + \overline{T}_{ij}) W_{ij} \right)}{\left(W_{ii} + \sum_{j \subset i} W_{ij} \right)} \quad (11)$$

where W_{ii} is the mean value of all W_{ij} of each CCD i

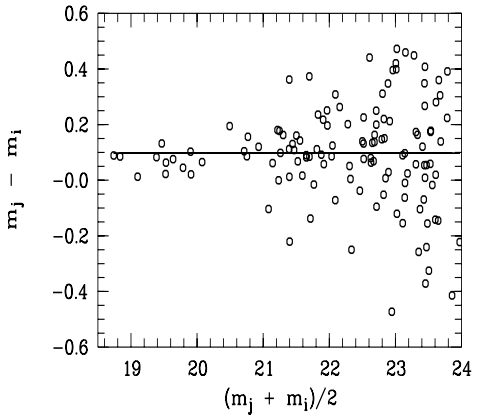

Fig. 8. Difference of magnitudes for common objects in two overlapping CCDs j and i. The solid line shows the linear fit for objects brighter than 22 mag which measures $\overline{T}_{ij} = m_j - m_i$

8.2. Results

To constrain the set of correction factors, Maddox used $\sum \delta C_i = 0$. In our case, we have re-observed several fields across the whole survey during the last observing run: 4 fields in B with TEK#31, 4 in V with TEK#36 and 5 fields in R with LOR#34. The seeing conditions were good

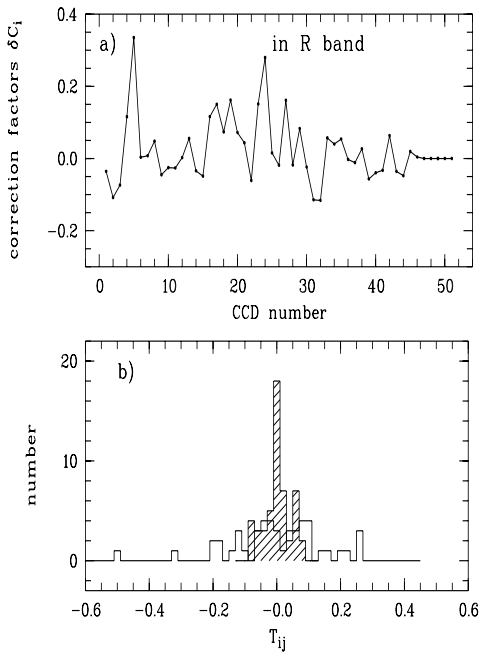

Fig. 9. The upper graph shows the estimated magnitude correction for the R filter to be applied to each CCD zero-point. The first 30 CCDs are fields observed at the 3.60 m and the remaining come from NTT observations. CCDs from 47 to 50 are used as reference frames with no correction factors which provide the constraints to the other frames The lower graph shows the histogram of $\overline{T}_{ij}$ before correction of the zero-point (empty histogram) and after correction (hashed histogram)

($FWHM \sim 1.0''$, $1.0''$, $0.8''$ in B, V, R respectively) and the photometric calibrations were performed with great caution. We use these fields as fixed references for the adjustments of the zero-points of the other frames. During this process, we detected systematic offsets in the initial V and R zero-points of the 3.6 m frames derived from calibration sequences (Sect. 6) when compared with the NTT reference frames: $\delta C_{3.60\,\mathrm{m}} - \delta C_{\mathrm{NTT}} = +0.10^{\mathrm{m}}$ in the R band, $\delta C_{3.60\,\mathrm{m}} - \delta C_{\mathrm{NTT}} = -0.10^{\mathrm{m}}$ in the V band. These shifts cannot be explained by a problem in the colour correction because the offsets are independent of the colour of the objects. Because of the absence of a similar shift in the B band, this effect cannot be attributed to the variation of the extinction coefficients due to the eruption of the Pinatubo volcano in 1991, which occurred when the observations switched from the 3.60 m telescope to the NTT telescope. To prevent the minimization method from introducing a gradient in the set of correction factors around the boundary between NTT and 3.60 m frames the equation systems in each band for the NTT and 3.60 m are processed separately.
First, we use $\sum \delta C_i = 0$ as a constraint for both systems. The solutions of the two systems provide the internal zero-point corrections to be applied to each CCD. Then,

we use the reference fields to derive the global magnitude shift of each ensemble of zero-points (3.60 m and NTT). These various steps allow us to adjust the two systems to the same zero-point. The resulting correction factors for the R band are shown in Fig. 9a. Each point defines one CCD and corresponds (with some gaps) to a sequence number (see figure captions). The iteration of Eq. (11) is stopped when the difference between the previous and new estimation ($\delta C_i^{n+1} - \delta C_i^n$) is smaller than $0.005^{\rm m}$ for all CCDs i. The typical number of required iterations is 10.
In Fig. 9b, we plot the histogram of initial and corrected $\overline{T}_{ij}$, $\overline{T}_{ij}^{\rm cor}$ defined as:

$$\overline{T}_{ij}^{\rm cor} = \overline{T}_{ij} + \delta C_j - \delta C_i. \quad (12)$$

In these histograms, we exclude the symmetric terms $\overline{T}_{ji} = -\overline{T}_{ij}$.
The rms scatter in the initial $\overline{T}_{ij}$ in B, V, R bands are respectively $0.11^{\rm m}$, $0.13^{\rm m}$, $0.14^{\rm m}$. After correction by δC_i, we reduce the scatter to $0.04^{\rm m}$ in all 3 bands.

8.3. Conclusion

These results demonstrate the efficiency of the method to reduce the dispersion between the CCD frames over the whole survey. They also allow us to estimate the dispersion in our magnitude system. In fact, if there was no error in the measures of magnitudes, $\overline{T}_{ij}$ would be equal to zero. The dispersion in the $\overline{T}_{ij}$ after adjustments gives a $0.04^{\rm m}$ error in our measured magnitudes in all 3 bands and is in good agreement with the $0.05^{\rm m}$ in the adaptive aperture magnitude uncertainty given by the simulations (see Sect. 4.2). To check the consistency of zero-point calibrations between the NTT and 3.60 m fields, we have applied a K-S two-sample test to the $B-R$ and $B-V$ colour distributions obtained as described in last section. The probability that the 2 distributions are drawn from the same parent distribution is 0.45 after correction of the systematic zero-point offsets between 3.60 m and NTT frames, it is 0.01 when the correction is not applied. This confirms that correction of the offsets in zero-point for the 3.60 m in R and V bands is necessary. Finally, there could be a systematic shift in our overall zero-point, but it would be within the error bars estimated from our individual zero-points (i.e. $\leq 0.05^{\rm m}$).

9. First results

9.1. Star sample

Byproducts of deep imaging surveys at different galactic latitudes are stellar samples in different directions of our galaxy at very faint magnitudes (Shanks et al. 1980; Kron 1980; Infante 1986; Metcalfe et al. 1991). In Figs. 10, 11, we show for our stellar sample the different colour histograms $B-R$, $B-V$, for three magnitude ranges in V. Note that the quasars are included in this sample. Also, at bright magnitudes ($V < 17$), a large fraction of stars are saturated, thus raising the uncertainty in the corresponding colours.
At faint magnitudes ($V \geq 18$), two stellar populations can be seen. Brightward of $V < 18$, one broad blue peak is present near $B-V \sim 0.5-0.6$. Faintward of this magnitude a second peak appears in the red part near $B-V \sim 1.4-1.5$. These results agree well with the other existing data (see Table 9.1 above). The red peak is interpreted as being nearby M stars belonging to the disk population. The blue sequence is interpreted as being stars belonging to the galactic halo (Robin & Crézé 1986).
These observations are listed in Table 9.1 for $V \leq 22$. The second column gives the colours used by the author, the third and fourth columns show the colours of the two peaks in this initial colour and the subsequent columns show the transformed position of the two peaks into the standard system Johnson-Cousins. The transformation equations are given in the corresponding publications, and for the Kron (1980) data we added the transformation equations given by Majewski (1992) as $(J-F) = 0.738(B-R) - 0.02$. Table 9.1 shows that our stellar color distributions are in good agreement with those resulting from other faint CCD surveys.

9.2. Galaxy sample

9.2.1. Galaxy counts

a) Counts and slopes
We present the differential galaxy counts based on the total 0.4 square degree of the survey in the R, V and B bands to limiting magnitudes of 23.5, 24.0 and 24.5 respectively. These limiting magnitudes are defined as the last magnitude bin ($\Delta m = 0.5$ mag) before the turn-off in the number counts. To these limits the galaxy catalogs contain about 13000, 12150 and 9500 objects in the R, V and B bands respectively. Note that there is no star-galaxy separation for $R \geq 22$ and no correction for stellar contamination is done because the expected number of stars at this galactic latitude ($b^{II} \simeq -83°$) is lower than 4% (corresponding to an offset of ~ 0.017 of the logarithmic number counts).
In Fig. 12, we show the differential galaxy number counts per square degree in 0.5 magnitude bins. The upper graphs show for each band the superimposed galaxy counts for all individual CCD fields. The dots displaced to the right of the columns of galaxy counts are the median counts offset by 0.2 mag for clarity. The error bars measure the 1σ rms field-to-field scatter. The field-to-field scatter is $\sim 20\%$ in the R band between $21 < R < 23.5$, $\sim 25\%$ in the V band between $21 < V < 24.$ and $\sim 30\%$ in the B band between $22 < B < 24.5$. These rms dispersions significantly exceed the expected Poisson variations in $\sqrt{N}$ because of galaxy-galaxy clustering (Arnouts & de Lapparent 1997). In the bright part, the large values of the scatter are

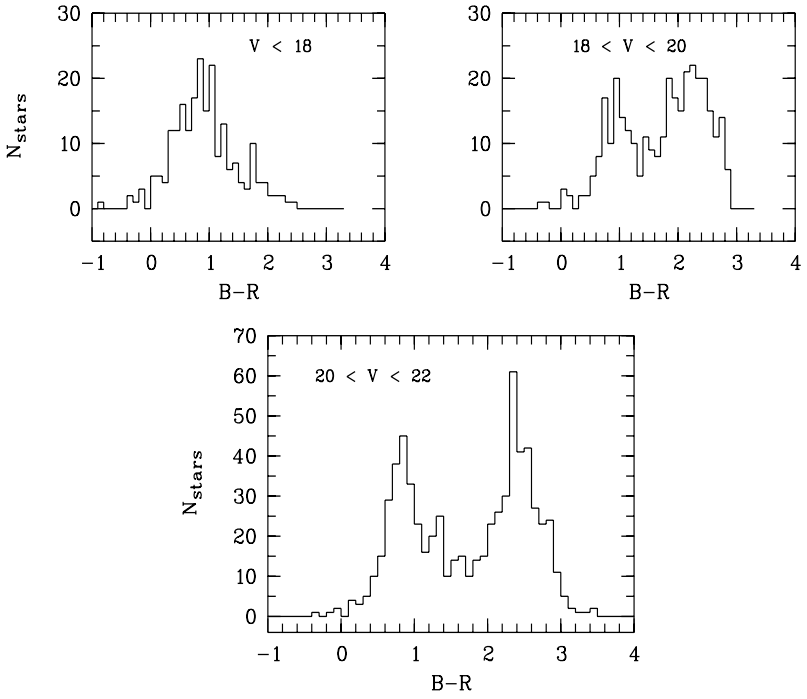

Fig. 10. $B-R$ colour histogram for the stars selected in three different ranges of V magnitude as specified within the graphs

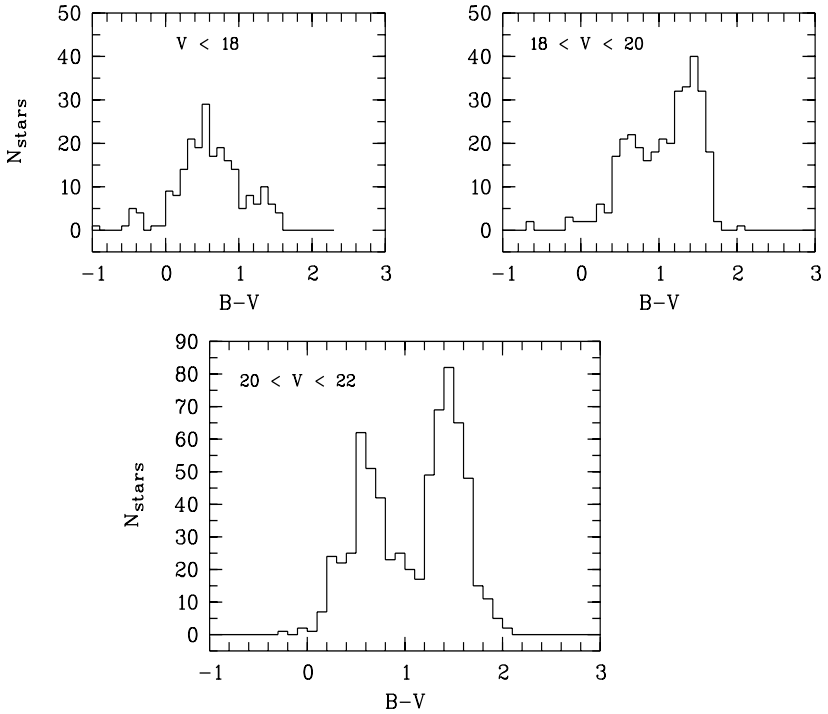

Fig. 11. same as Fig. 10 for $B-V$ colour

Table 4. Stellar colour peak for $V \leq 22$

Reference	Observed colours	blue peak	red peak	blue peak			red peak		
				$B-V$	$B-R$	$V-R$	$B-V$	$B-R$	$V-R$
Kron et al. (1980)	$J-F$	0.65	1.75	0.50	0.90	0.40	1.50	2.40	0.90
Shanks et al. (1980)	$J-R$	1.0	2.2	0.6			1.6		
Infante (1986)	$J-r$	0.9	2.3	0.6			1.5		
Metcalfe et al. (1991)	$(B-R)_{\rm ccd}$	1.0	2.2		1.12			2.46	
This work				0.55	0.90	0.35	1.45	2.40	0.95

essentially due to the small number of bright galaxies per CCD frame. The lower graphs give the median number counts. In these graphs the error bars are given as:

$$\sigma = \sigma_{\rm field-to-field}/\sqrt{N_{\rm field}}. \quad (13)$$

The differential number counts (in $\deg^{-2}$ 0.5 mag^{-1}) are fitted by a power law in the same magnitude range as Metcalfe et al. (1991) for the R and B magnitudes. The exponent of the fit in the three bands are measured by a least squares fit in the $\log N -$ mag plots. These fits are shown by solid lines in the lower graphs of Fig. 12 and are parameterized as follow:

$$N_{\rm gal} = 10^{(0.460\pm0.02)B} \times 10^{-7.01\pm0.39} \quad (14)$$

for $20.5 \leq B \leq 24.5$

$$N_{\rm gal} = 10^{(0.384\pm0.02)V} \times 10^{-5.03\pm0.47} \quad (15)$$

for $20.0 \leq V \leq 24.0$

$$N_{\rm gal} = 10^{(0.367\pm0.02)R} \times 10^{-4.42\pm0.47} \quad (16)$$

for $20.0 \leq R \leq 23.5$.

In Table 9.2.1, we summarize the results of previous CCD surveys on galaxy counts in the visible bands. Our slopes are in good agreement with the other works.

In Fig. 12, we detect two magnitude bins between $21.0 \leq B \leq 22.0$ where the density systematically decreases and this effect is seen in the three bands (in the intervals $20.5 \leq V \leq 21.5$ and $20.5 \leq R \leq 21.5$). First of all, to see if this gap was caused by inhomogeneities in the projected distributions, we examined the angular distribution (RA, Dec) in different magnitude intervals, but no particular feature in the clustering of the projected distributions was visually detected. This investigation will be pursued quantitatively in a forthcoming study of the two-point angular correlation function for these data (Arnouts & de Lapparent 1997).

b) Counts comparison

In Figs. 13-15 we compare the differential number counts from our data with those from the other CCD surveys. For the data given in other systems than the standard Johnson-Cousins system, we apply the different transformations provided by the authors. For the data from Metcalfe we apply a transformation only for the B band as $B = B_{\rm ccd} + 0.15$.

Table 5. The galaxy number count exponents for several CCD photometric surveys

Reference	B	V	R
Tyson (1988)[a]	0.45		0.39
Lilly et al. (1988)[b]	0.38		
Metcalfe et al. (1991)[c]	0.49		0.37
Driver et al. (1995)[d]	0.44	0.40	0.37
Smail et al. (1995)[e]		0.40	0.32
This work[e]	0.46	0.38	0.37

a: in the $B_{\rm J}$, R, I CCD photometric system
b: in the AB photometric system
c: in their CCD photometric system
d: in the KPNO system
e: in the Johnson-Cousins system.

For the data from Tyson, the transformation equations are not given. By default we use the transformations into the photographic system $(b_{\rm J}, r_{\rm F})$ given in Metcalfe et al. (1991) combined with the transformations from photographic bands to the standard system given by Shanks et al. (1984). We obtain the approximate transformations defined as $B = B_{\rm Tyson} + 0.27$ and $R = R_{\rm Tyson} - 0.07$.

For the data from Driver no transformations are done because the color terms are small. Except for Metcalfe et al. (1991), these other works are significantly deeper than our data, and the number counts at very faint magnitudes ($B \geq 25$ and $R \geq 23.5$) are corrected for confusion.

Figures 13, 14, 15 show that our counts in B and R are in good agreement with the results from Metcalfe et al. (1991) in both the slope and the amplitude of the logarithmic number counts in the red band but a small shift in the blue band exists as we will see below in the discussion of the colour distributions (Sect. 9.2.2). The R number counts of our survey are significantly higher ($> 3\sigma$) than those from Tyson in the common range of magnitudes. This difference has been interpreted by Tyson (1988) as being due to the a priori choice of fields devoid of bright galaxies, and Metcalfe et al. (1991) suggest that this difference can originate from the use of isophotal magnitudes by Tyson (1988) in contrast to the "total" magnitudes used

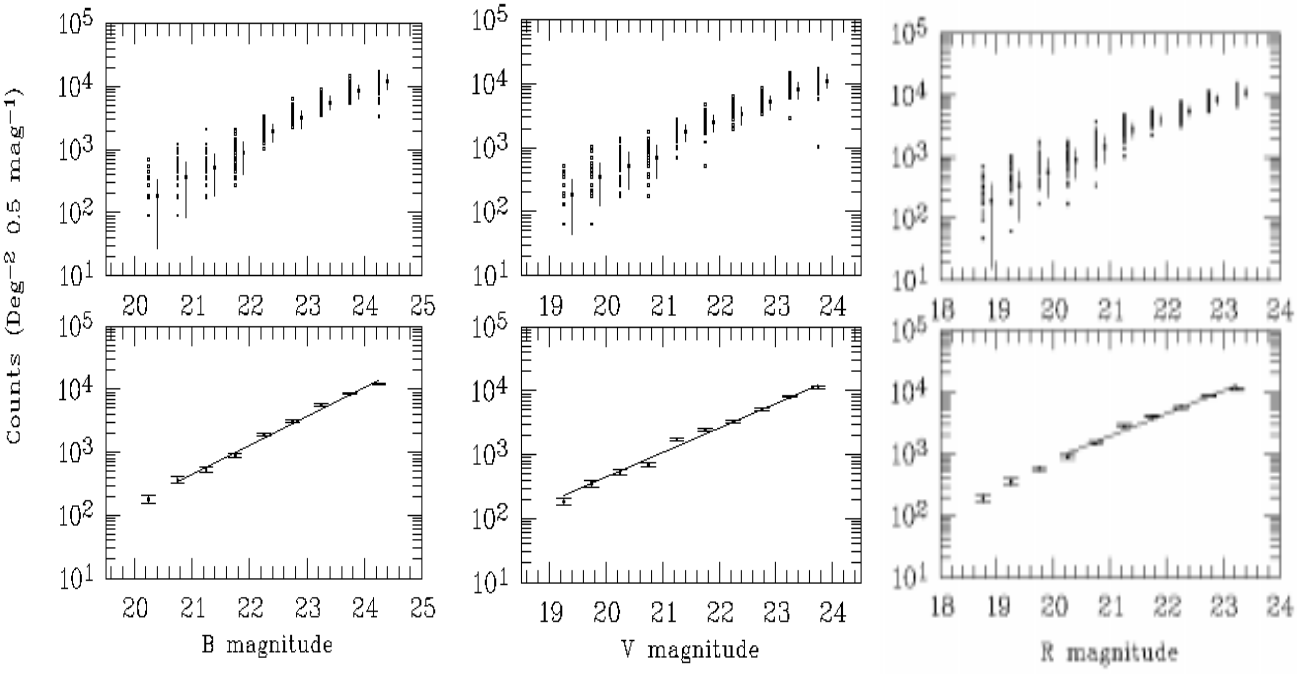

Fig. 12. Galaxy number-magnitude counts by square degree per 0.5 mag interval in the B (left), V (center) and R (right) bands. The upper graph shows the counts for each observed CCD field and the median values with error bars given as the σ field-to-field fluctuation. The lower graph shows the median number count value in each bin. The error bars are given by Eq. (13). The solid line is the estimated slope by least squares fit. **a)** Galaxy counts in B band; **b)** Galaxy counts in V band; **c)** Galaxy counts in R band.

by the others authors. The data of Driver et al. (1994) also show a small deficit in galaxy number counts compared to ours at the $\sim 3\sigma$ level. Driver specifies that the Hitchhiker data suffers from a calibration uncertainty, so a small shift in zero-point could explain the deficit in the three visible bands but this effect does not alter the slopes of the counts. In the data from Smail et al. (1995), the plotted points correspond to the average of two single fields. Their V counts are in very good agreement with ours but their R counts show a significant number excess by a factor of about 1.2 compared with all the others authors below $R < 24$.

Finally we compare our deep counts with the recent bright galaxy counts in B and R bands performed by Bertin & Dennefeld (1997). These counts are in good agreement with ours and we use them to normalize the non-evolving model kindly provided by M. Fioc. Bertin & Dennefeld (1997) suggest: $\Phi^\star = 0.0035\, h_{50}^3$ Mpc^{-3} mag^{-1} in the B band (estimated at $B \sim 19^{\rm m}$), $\Phi^\star = 0.0033\, h_{50}^3$ Mpc^{-3} mag^{-1} in R band and we adopt an intermediate value of $\Phi^\star = 0.0034\, h_{50}^3$ Mpc^{-3} mag^{-1} in the V band (h_{50} is defined by $H_0 = 50\, h_{50}$ km s^{-1} Mpc^{-1}). The other parameters of the luminosity function come from Guiderdoni & Rocca-Volmerange (1990): $\alpha \sim -1.0$ and $M_B^\star \sim -20.6$.

9.2.2. Galaxy colours

In this section, we present the first results of the colour distributions for our galaxy catalogue in the B, V and R bands. As shown in Fig. 7, there is a large fraction of objects identified in all 3 filters for $B < 24$ ($\sim 95\%$ of objects). In the following, we restrict the sample to these 7500 common objects.

In Figs. 16-18 we plot the mean observed colours $B-R$, $B-V$, $V-R$ as a function of magnitude for the 7500-object sample. The solid lines draw the 1σ envelope of the measured colours, σ being the rms dispersion of the colour histogram within the corresponding magnitude bin. This envelope is larger in $B-R$ than in $B-V$ and $V-R$ because the expected colour in $B-R$ varies in a large range for the different galaxy types. The $B-R$ and $B-V$ colours clearly show a tendency to become bluer at fainter magnitude as first observed by Kron (1980) and subsequently confirmed by several groups (Tyson 1988; Metcalfe et al. 1991, 1995). At $V \leq 21.5$, the typical mean colour is $B-R \sim 1.55$ and a blueing shift to $B-R \sim 1.0$ is seen between $22 < V < 24$. The same tendency is visible in the $B-V$ colour distribution. It decreases from $B-V \sim 1.05$ at $V < 22$ to $B-V \sim 0.6$ at $V = 24$. Note that in Fig. 16 , at $B > 24$ mag, the completeness level drops to $\sim 60\%$ (see Fig. 7) and the mean colours $(B-R)$ and $(B-V)$ become redder due to the incompleteness in the R and V bands where

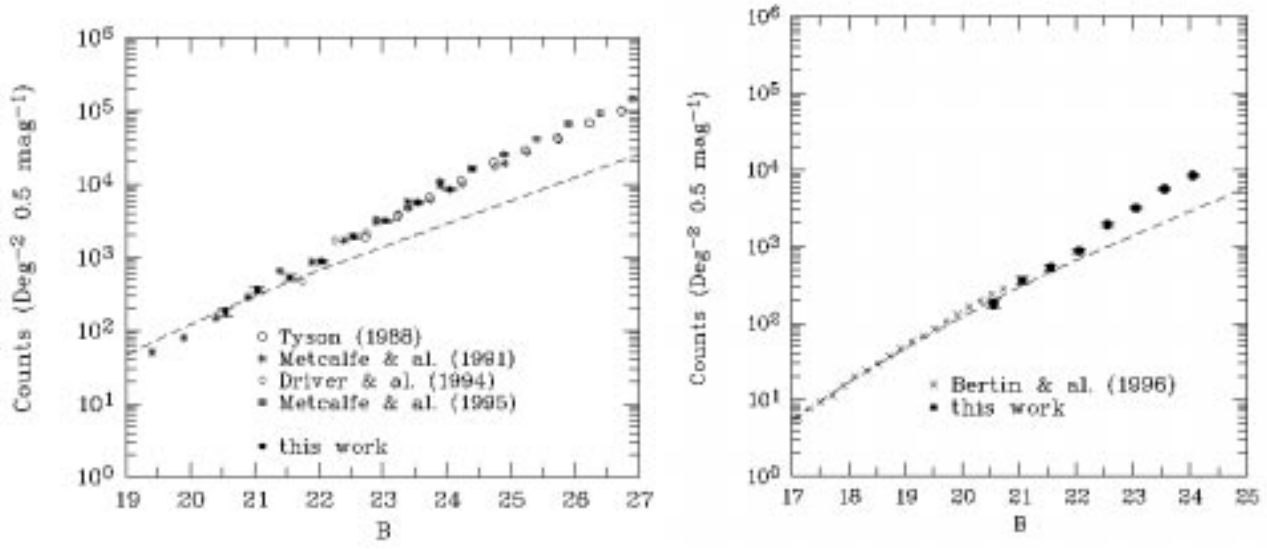

Fig. 13. Comparison with others published galaxy number counts transformed into the B Johnson filter. The error bars for our data show the σ estimated in Eq. (13). The dashed line shows the differential number counts expected for a non evolving model using a $\Phi^{\star}$ normalized to the bright galaxy number counts from Bertin & Dennefeld (1997) as described in the text. **a)** Comparison with others deep CCD galaxy number counts. **b)** Comparison with bright photographic galaxy number counts from Bertin & Dennefeld (1997)

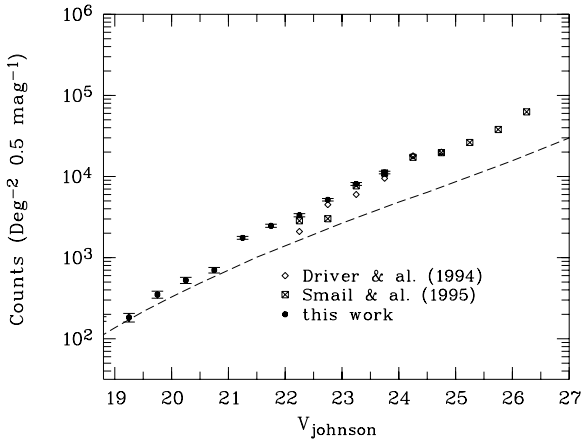

Fig. 14. Same as Fig. 13 in the V Johnson filter

only the brighter objects are identified and contribute to shift the colour toward redder colours.

In contrast, the $(V-R)$ colours in Figs. 16-18 show no evidence of colour evolution with magnitude up to $V \leq 24$. The same stability is obtained by Driver et al. (1994).

In addition, we compare our observed mean colours $B-R$ with those from Metcalfe et al. (1991, 1995) and our mean $V-R$ colours with those of Smail et al. (1995). Metcalfe et al's $B-R$ colours are systematically 0.1 mag redder than ours. Half of this shift is expected due to reddening in the fields of Metcalfe et al. (Metcalfe 1995). Comparison with the $V-R$ colours of Smail also show a small offset, but the restricted overlap in the magnitude ranges covered does not allow us to draw any firm conclusions about the agreement between the data sets.

10. Conclusion

We have obtained CCD photometry for 9500, 12150, 13000 galaxies in the B, V, R (Johnson-Cousins) filters to limiting magnitudes of 24.5, 24.0, 23.5 respectively over an area

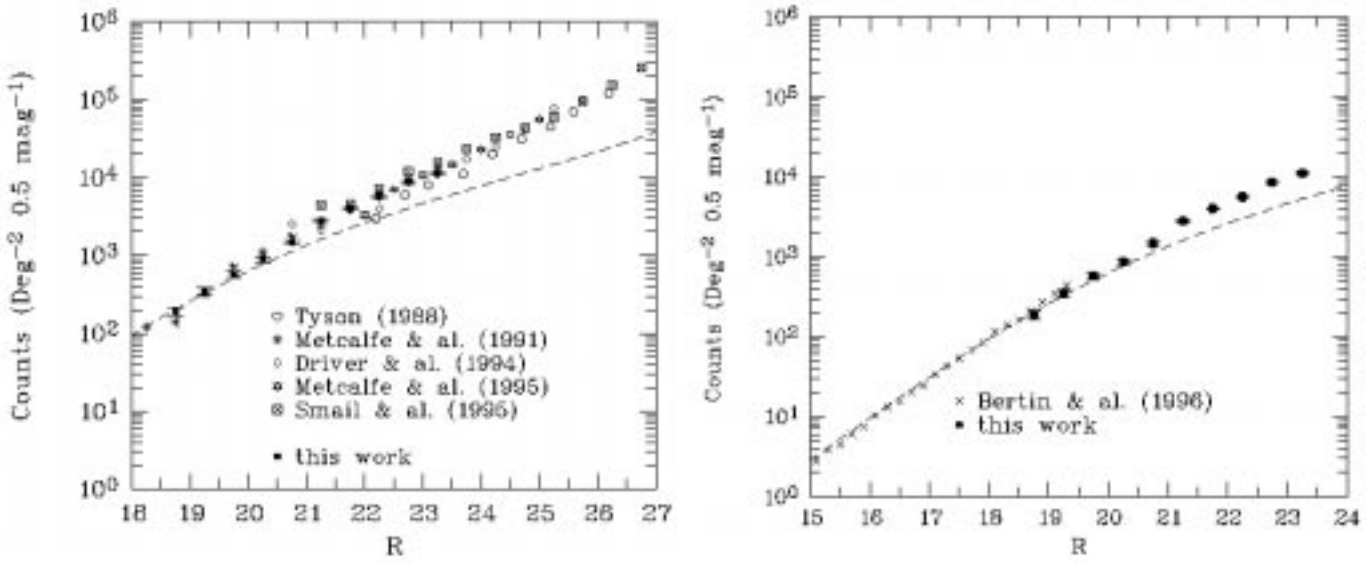

Fig. 15. Same as Fig. 13 in the R Cousins filter. **a)** Comparison with others deep CCD galaxy number counts. **b)** Comparison with bright photographic galaxy number counts from Bertin & Dennefeld (1997)

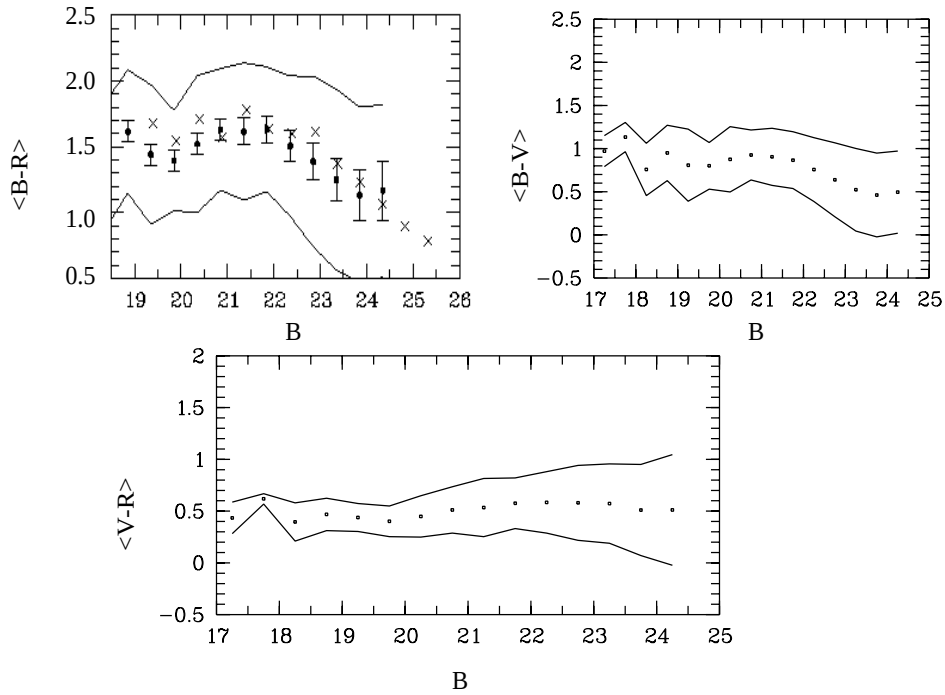

Fig. 16. Galaxy mean colours as a function of 0.5 bin of B magnitude. The solid lines represent the 1σ envelope of the measured colours. The upper left graph shows the mean $B-R$ from our data (filled circles) and from the data of Metcalfe et al. (1991, 1995) (crosses). The error bars give the quadratic errors in the magnitudes obtained from the simulations

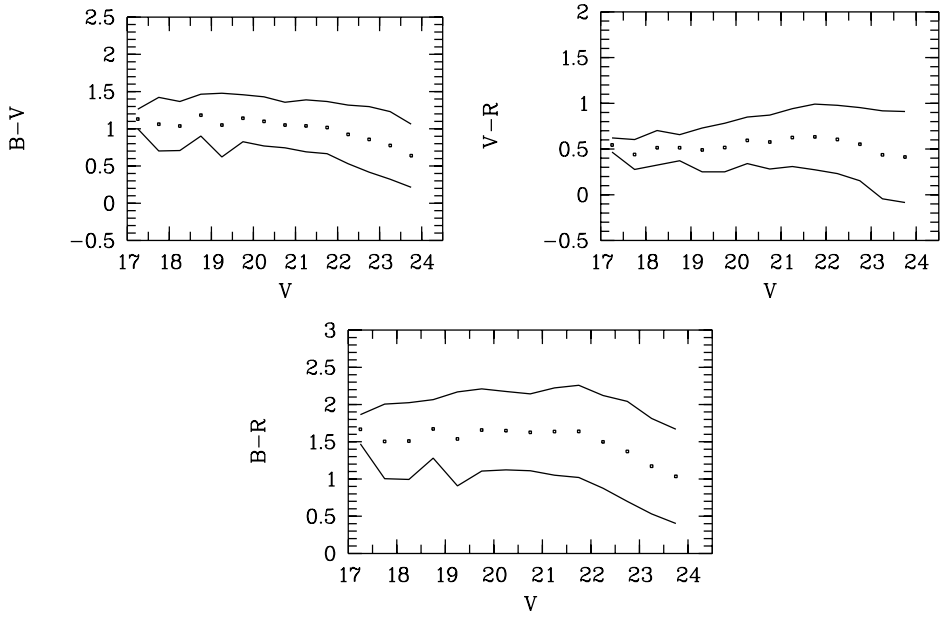

Fig. 17. same as Fig. 16 for V magnitude

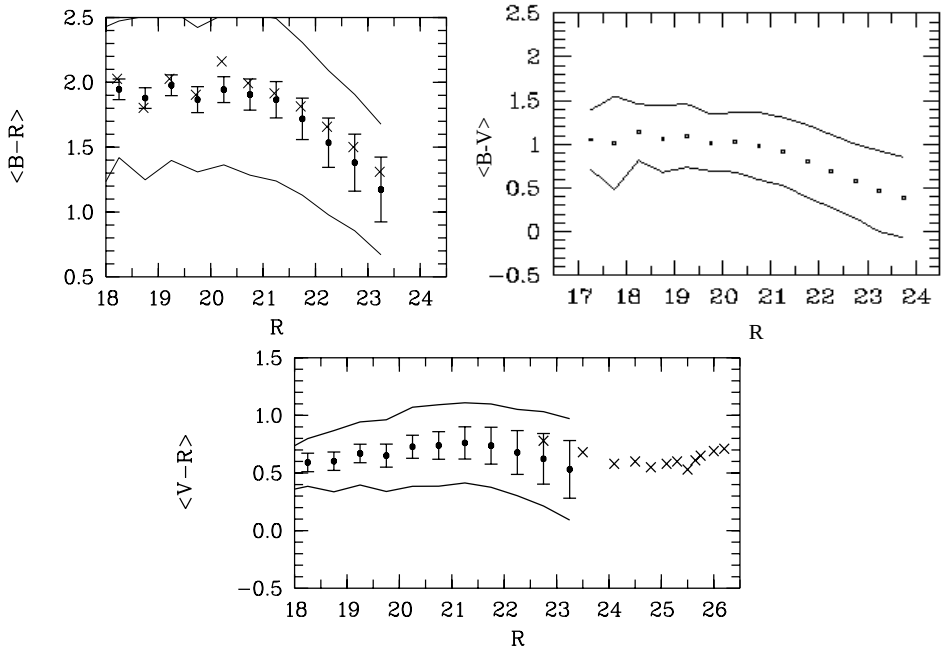

Fig. 18. same as Fig. 16 for R magnitude. The upper left graph shows the mean $B-R$ from our data (filled circles) and from the data of Metcalfe et al. (1991, 1995) (crosses). The lower graph compares the mean $V-R$ from our data (filled circles) with those from Smail et al. (1995) (crosses)

of $0.4\,\mathrm{deg}^2$ near the southern galactic pole. Automatic procedures were designed in order to reduce the data in an homogeneous fashion. The main steps used in obtaining the photometric catalogue are summarized as follows:
i) We have applied the standard pre-reduction techniques of bias subtraction, flat-fielding by median filtering and cosmic-ray removal.
ii) Because different CCDs were used over the course of the programme, a large set of colour equations and zero-points were measured in order to provide reliable calibrations for the survey. We could then transform all instrumental magnitudes into the Johnson-Cousins standard system.
iii) The survey data is a mosaic of $\simeq$ 50 CCD frames in each band which have $\sim$ 1 arcmin overlaps. We could therefore perform an internal and global re-adjustment of the zero-point of each CCD over the whole survey. In this way, we reduce the zero-point field-to-field scatter from ~ 0.11 mag to ~ 0.04 mag, in agreement with the photometric uncertainty estimated using simulated images (0.05^{m} for $R \leq 22$ and 0.2^{m} at fainter magnitudes). We therefore reduce the internal dispersion in our photometry to the intrinsic dispersion resulting from the limitations of the photometric package.
iv) Accurate astrometry is performed for each CCD frame. The positional accuracy is $0.1''$ for objects with $R \leq 22$ and increases to $0.3''$ at fainter magnitudes, as estimated from objects located in the overlapping edges of the CCDs.
v) Measurement of the object colours is performed by matching the astronomical coordinates in each band with a tolerance of $1.2''$ in position offset. The colour completeness with respect to the B band (fraction of B objects with R and V counterparts) is greater than 95% up to $B \leq 24$ and drops to 60% at 24.5. The colour uncertainties are estimated as the corresponding quadratic sum of the errors in the photometric magnitudes ($\sigma_{(B-V),(V-R),(B-R)} \leq 0.07$ for $R \leq 22$ and $\sigma_{(B-V),(V-R),(B-R)} \leq 0.28$ for $R \geq 22$).
vi) The star-galaxy separation is performed using a neural network and is expected to be close to a 95% success rate for $R \leq 22$. We use the R band for the star/galaxy separation because it is our deeper band, it was observed with the best seeing conditions, and it is used for the spectroscopic selection. At $R \geq 22$, no separation is done due to the small fraction of faint stars expected ($\sim 4\%$) at the high galactic latitude of the survey ($b^{II} \sim -83°$).

The first results from the large photometric catalogue show that:
i) The galaxy counts in apparent magnitude and their slopes in logarithmic scale are in good agreement with previous CCD and photographic surveys and show an excess in all 3 bands with respect to the non-evolving models.
ii) The $(B-V)$ and $(B-R)$ median galaxy colours show a blueing shift of ~ 0.5 mag from $B \sim 22$ to $B \sim 24.5$. In contrast, the $(V-R)$ median colour is nearly constant up to $R \sim 23.5$.
iii) The galaxy counts are well fitted by a non-evolving model for $R \leq 20.$ using a $\Phi^\star$ derived from the new bright galaxy counts of Bertin & Dennefeld (1997).
iv) Two peaks in the stellar distributions are present in good agreement with the Robin & Crézé (1986) model of the galactic disk and halo.
The next step in the study of this photometric sample is the analysis of the angular correlation function $\omega(\theta)$ at faint magnitude (Arnouts & de Lapparent 1997). This work will provide information about the galaxy clustering ever a wide range of scales and apparent magnitudes. The high completeness rate in colour should also allow to further characterize the properties of the faint blue galaxies. Together with the photometric data, the redshift survey of $\sim$ 700 galaxies with $R \leq 20.5$ will provide a multicolour optical luminosity function in the redshift range $0.1 \leq z \leq 0.5$. Altogether, these data will allow us to address the issue of the evolution of galaxies with $B \leq 22$. The photometric and redshift catalogues will also be complemented by a spectral classification of all galaxies with $R \leq 20.5$ (Galaz & de Lapparent 1996) and will thus provide an unique database for studying the variations in the galaxy properties as a fonction of environment and redshift.

Acknowledgements. We are grateful to the European Southern Observatory for the large amount of observing time and the corresponding logistic support which allowed to perform this observing programme in good conditions and to bring it to completion. We are grateful to Dr. P. Leisy for kindly providing us his cosmic removal algorithm, and to M. Fioc and Dr. B. Rocca-Volmerange for kindly providing us the non-evolving model to fit the differential galaxy number counts. We thank Dr. C. Willmer for fruitful discussions. We also thank the referee Dr. N. Metcalfe for his scientific comments and linguistic corrections.

References

Arnouts S., de Lapparent V., 1997 (in preparation)
Bellanger C., de Lapparent V., Arnouts S., et al., 1995a, A&AS 110, 159
Bellanger C., de Lapparent V., 1995b, ApJL 455, L103
Bertin E., 1996, PhD thesis, IAP
Bertin E., Arnouts S., 1996, A&AS 117, 393 (BA96)
Bertin E., Dennefeld M., 1997, A&A 317, 43
Broadhurst T.J., Ellis R.S., Shanks T., 1988, MNRAS 235, 827
Broadhurst T.J., Ellis R.S., Koo D.C., Szalay A.S., 1990, Nat 343, 396
Broadhurst T.J., Ellis R.S., Glazebrook K., 1992, Nat 355, 55
Bruzual A.G., 1983, ApJ 273, 105
Burki G., Rufener F., Burnet M., et al., 1995, A&AS 112, 383
Buzzoni B., Delabre B., Dekker H., et al., 1984, The Messenger 38, 9
Colless M.M., Ellis R.S., Taylor K., Hook R.N., 1990, MNRAS 244, 408
Colless M.M., Ellis R.S., Broadhurst T.J., Taylor K., Peterson B.A., 1993, MNRAS 261, 19
Cowie L.L., Songaila A., Hue E.M., 1991, Nat 354, 460
Dalcanton J.J., 1993, ApJ 415, L87

da Costa L.N., Geller M.J., Pelligrini P.S., et al., 1994, ApJ 424, L1
Dekker H., d'Odorico S., Kotzlowski H., et al., 1991, The Messenger 63, 73
de Lapparent V., Geller M.J., Huchra J.P., 1986, ApJ 302, L1
de Lapparent V., Geller M.J., Huchra J.P., 1991, ApJ 369, 273
d'Odorico S., 1990, The Messenger 61, 51
Driver S.P., Phillipps S., Davies J.I., Morgan I., Disney M.J., 1994, MNRAS 266, 155
Efstathiou G., Bernstein G., Katz N., Tyson J.A., Guhathakurta P., 1991, ApJ 380, L47
Geller M.J., Huchra J.P., 1989, Sci 246, 897
Guiderdoni B., Rocca-Volmerange B., 1990, A&A 227, 362
Glazebrook K., Ellis R., Colless M., et al., 1995a, MNRAS 273, 157
Glazebrook K., Ellis R., Santiago B., Griffiths R., 1995b, MNRAS (preprint)
Graham J., 1981, PASP 93, 29
Infante L., 1986, PASP 98, 360
Koo D.C., Kron R.G., 1992, ARA&A 30, 613
Koo D.C., Gronwall C., Bruzual G.A., 1993, ApJ 415, L21
Kron R.G., 1980, ApJS 43, 305
Landolt A.U., 1992, AJ 104, 340
Leisy P., 1994 (private communication)
Lilly S.J., Cowie L.L. and Gardner J.P., 1991, ApJ 369, 79
Majewski S.R., 1992, ApJS 78, 87
Maddox S.J., Efstathiou G., Sutherland W.J., 1990a, MNRAS 246, 433
Maddox S.J., Sutherland W.J., Efstathiou G., Loveday J., Peterson B.A., 1990b, MNRAS 247, 1p
Metcalfe N., Fong R., Shanks T., Jones L.R., 1991, MNRAS 249, 498
Metcalfe N., Fong R., Shanks T., Jones L.R., 1995, MNRAS
Metcalfe N., 1995 (private communication)
Moffat A.F.J., 1969, A&A, 3, 455
Ostriker J.P., 1990, in The Evolution of the Universe of Galaxies, Kron R. (ed) p.25
Revenu B., de Lapparent V., 1992 (private communication)
Robin, Crézé, 1986, A&A 157, 71
Roeser, S., Bastian, U., 1991, PPM Star Catalogue, Spektrum Akademisher Verlag. Heidelberg, Berlin, New York
Ramella M., Geller M.J., Huchra J.P., 1992, ApJ 384, 396
Roche N., Shanks T., Metcalfe N., Fong R., 1993, MNRAS 263, 360
Rocca-Volmerange B., Guiderdoni B., 1990, MNRAS 247, 166
Schwarz H.E., Melnick J., 1993, The ESO Users Manual
Seldner M., Siebers B., Groth E. J., Peebles P.J.E., 1977, AJ 82, 249
Shanks T., Phillipps S., Fong R., 1980, MNRAS 191, 47p
Shanks T., Stevenson P.R.F., Fong R., McGillivray H.T., 1984, MNRAS 206, 767
Smail I., Hogg D.W., Yan L., Cohen J.G., 1995 (preprint)
Tresse L., Hammer F., Le Fèvre O., Proust D., 1993, A&A 277, 53
Tyson J.A., 1988, AJ 96, 1
West R., Kruszewski A., 1981, Irish Astron. J. 15, 25
Yoshii Y., Takahara F., 1988, ApJ 326, 1